Single-Janus Rod Tracking Reveals the “Rock-and-Roll” of Endosomes in Living Cells

Yuan Gao,[†] Stephen M. Anthony,[‡] Yi Yi,[†] Wenqian Li,[†] Yanqi Yu,[†] Yan Yu[†]*

[†]Department of Chemistry, Indiana University, Bloomington, Indiana 47405, United States

[‡]Department of Bioenergy and Defense Technology, Sandia National Laboratories, Albuquerque, New Mexico 87123, United States

ABSTRACT

Endosomes in cells are known to move directionally along microtubules, but their rotational dynamics have rarely been investigated. Even less is known, specifically, about the rotation of non-spherical endosomes. Here we report a single-Janus rod rotational tracking study to reveal the rich rotational dynamics of rod-shaped endosomes in living cells. The rotational reporters were Janus rods that display patches of different fluorescent colors on the opposite sides along their long axes. When wrapped tightly inside endosomes, the shape and optical anisotropy of these Janus rods enable the simultaneous measurements of all three rotational angles (in-plane, out-of-plane, and longitudinal) and the translational motion of single endosomes with high spatiotemporal resolutions. We demonstrate that endosomes undergo in-plane rotation and rolling during intracellular transport and that such rotational dynamics are driven by rapid microtubule fluctuations. We reveal for the first time the “rock-and-roll” of endosomes in living cells, and how the intracellular environment modifies such rotational dynamics. This study demonstrates a unique application of Janus particles as imaging probes in the elucidation of fundamental biological questions.

INTRODUCTION

Cells internalize materials into intracellular vesicular compartments known as endosomes.[1, 2] Endosomes are carried on the cytoskeleton by molecular motors, sorted, and delivered to intracellular locations.[3, 4] The trafficking of endosomes regulates many essential cell functions, from migration to proliferation, and many devastating human diseases are caused by defects in this process.[5, 6] Our ability to understand the pathogenesis of those diseases and identify therapeutic targets critically depends on the availability of methods to dissect the dynamics and mechanisms of endosome trafficking.

Single-particle imaging and tracking has been used widely to investigate endosome trafficking in living cells.[7, 8, 9] In theory, one can precisely quantify the dynamics of single endosomes and their interaction with subcellular structures by following their trajectories. In fact, studies that examined the translational motion of endosomes have led to many breakthroughs in understanding endosome transport.[10, 11, 12, 13, 14] However, as research progressed from *in vitro* systems where microtubules are reconstructed on glass surfaces to studies inside living cells, measuring only the translational dynamics of endosomes becomes insufficient. It is expected that the three-dimensional interactions experienced by endosomes travelling inside cells will cause rotation, as well as translational motion, and that such rotational motion could therefore provide valuable clues about the nature of these interactions. Yet, little is known about how endosomes rotate in cells or how their rotation correlates with the intracellular environment. So far, only a handful of studies have monitored endosome rotation in intracellular trafficking, and these have all been done with gold nanorods as imaging probes. Two of the studies, one by Xiao *et al*.[15] and the other by

Chaudhari *et al*.[16] were merely intended to demonstrate the feasibility of the technique rather than investigating the transport of endosomes. Gu *et al*. reported the rotation of gold nanorods inside endosomes during axonal transport.[17] However, none of those methods allow for the measurement of the rod rotation around the longitudinal axis because of the optical symmetry of gold nanorods around that axis.

In this study, we demonstrate a new imaging method to simultaneously measure all three components of rotational motion (in-plane, out-of-plane, and longitudinal) and translation of rod-shaped endosomes in living cells. This method uses a novel type of dual-color Janus rods as imaging probes. These Janus rods, made with a "sandwich" microcontact printing procedure, display two patches of distinct fluorescence on the opposite sides along their long axes. Once internalized into endosomes, the shape and optical anisotropy of the Janus rods allow direct visualization and measurement of the rotational and translational dynamics of single endosomes in cells. This rotational tracking method uses wide-field fluorescence microscopy, which is more suitable for live cell imaging than the interference-based methods used with gold nanorods. We show that endosomes undergo in-plane rotation and rolling during intracellular transport. When the rod-containing endosomes pause on microtubules, they rotate and roll due to the rapid fluctuations of the microtubule network. In contrast, they undergo little rotation while being actively transported by molecular motors along microtubule tracks. Because some endosomes in cells exhibit elongated shapes[18] and some intracellular organelles (such as mitochondria) that undergo motor-driven transport are also rod-shaped,[19] our results shed new insights into understanding the transport dynamics of such structures in cells.

RESULT AND DISCUSSION

Janus rods used in this study were made from silica rods that are 0.44±0.06 μm (ave±s.d.) in diameter and 1.43±0.09 μm (ave±s.d.) in length (Fig. S1a).[20, 21] To render the silica rods optically anisotropic, we created, on each rod, two fluorescent patches on the opposite sides of the long axis, using a "sandwich" microcontact printing method (Fig. 1a).[22, 23] In this procedure, a monolayer of silica rods was pressed in between two PDMS stamps that were pre-inked with polyethylenimine (PEI) Alexa Fluor-568 or PEI Alexa Fluor-647. The fluorescently labeled PEI was transferred onto the opposite sides of individual rods upon contact.

The dual-color Janus rods appear as two parallel long patches in 2D projection epifluorescence images (Fig. S1b). The rotation and location of single Janus rods can be measured based on the orientation and location of each patch, and the inter-patch distance. The three rotational angles are referred to as the in-plane (azimuthal) angle φ, out-of-plane (polar) angle δ, and rolling angle θ (Fig. 1b). The in-plane angle φ was determined from the orientations of the long axes of each pair of patches (Fig. 1c). The rolling angle θ was calculated from the projected inter-patch distance: $\theta = \cos^{-1}(d/d_{max})$, in which d is the vertical distance between a pair of fluorescent patches at any given orientation in a 2D projection image, and d_{max} is the physical distance between the two patches, obtained as the maximum of d when a Janus rod samples all rolling angles during imaging (Fig. 1d). Because we cannot differentiate in projected wide-field fluorescence images rolling angles that are either above or below the imaging plane, we can only obtain θ angles from 0 to π using this method. The out-of-plane rotational angle δ can be calculated using this equation: $\delta = \cos^{-1}(l/l_{max})$, in which l is the projection length of a patch at any given orientation, and l_{max} is the physical length of the same patch, which is obtained when a

rod lie flat within the x,y plane ($\delta = 0$). In our experiments, the rods inside cells were not observed to exhibit any out-of-plane rotation, likely because microtubules in the adherent cells are oriented mostly parallel to the surface. The tracking uncertainties in our living cell experiments were 2±1° for in-plane angle φ, 4±2° for rolling angle θ, and 10±4 nm for translational motion (see SI and Fig. S2).

For a Janus rod to faithfully report the rotation of the endosome that it resides in, the rod must not be free to rotate inside the endosome. This was ensured through ligand-receptor binding between the Janus rods and endosomes. The COS-7 cells used in this study were transfected to express Fcγ receptors and Janus rods were coated with the corresponding ligand, immunoglobulin G (IgG) antibody. Fcγ receptors bind to the IgG antibodies and initiate cellular internalization of large particles.[24, 25] Owing to the specific ligand-receptor binding, ≈ 70% of the IgG-coated Janus rods were internalized compared to < 10% of rods without IgG (Fig. S3a). More than 80% (57 out of 71) of the internalized rods remained tightly wrapped inside endosomes at 45 min after the addition of rods to cells, which was the time window of our live cell imaging (Fig. S3b, c). Given the existence of ligand-receptor conjugation and the tight fit of the endosome membrane, rotation of Janus rods inside endosomes is unlikely.

Endosomes containing Janus rods were observed to move directionally over distances of a few hundred nm to a few μm, but frequently pause and switch moving directions in between episodes of directional motion (Fig. 2a, Movie S1). Such translational movements are characteristic of the active transport of endosomes driven by kinesin and dynein motors along microtubules.[11, 26] As the rods travelled along, they also rotated both in-plane and longitudinally (rolling) (Fig. 2a insets). The rotation and rolling were not continuous, but

occurred in short bursts that each lasted a few seconds. Moreover, each brief episode of rotation or rolling was mostly unidirectional. For instance, the rod shown in Fig. 2a rolled in one direction for 42.7° from 23.5 s to 27.5 s, and rotated in-plane for 16.8 ° between 52 s and 56 s.

When we matched the orientation of Janus rods to their translational trajectories, we noticed two interesting phenomena. First, during episodes of directional transport that appeared similar translationally, the rods were oriented in drastically different ways. As shown in Fig. 2c-d, the Janus rod was oriented with its long axis nearly parallel to the moving direction during a segment of directional motion between 0 s and 5.5 s (referred to as $M_{//}$, Fig. 2c). The average angle between the long-axis of the Janus rod and its moving direction, defined as angle α (Fig. 2b), was 9.0±12.2°. In contrast, the same Janus rod was almost perpendicular to the moving direction during another similar episode from 52 to 56 sec, with an average angle α of 60.1±16.8° (referred to as $M_{\perp}$, Fig. 2d). When the rod paused in between episodes of directional transport, it maintained its orientation (referred to as M_0, Fig. 2e). The second interesting phenomenon observed was that the rotation and rolling of rods appeared to occur during specific types of translational behavior (Fig. 2).

To quantitatively identify the correlation between the rotational and translational dynamics of the rods, we plotted the x, y-displacements, in-plane angle φ, and rolling angle θ of the rod shown in Fig. 2 (Fig. 3a-b). $M_{//}$ and $M_{\perp}$ movements and M_o pauses were identified based on both the angle α and translational displacement; episodes of rapid unidirectional rotation and rolling were distinguished from stochastic noise based on the amplitude of angular change (see details in Experimental Section SI, Fig. S4a, b). After highlighting the different translational and rotational movements, we observed an obvious

correlation between them. It is evident that the rod exhibited active in-plane rotation during the $M_{\perp}$ movements when the rod was oriented nearly perpendicular to its moving direction. Active rolling occurred when the rod paused (M_o). In contrast, the rod exhibited no active rotation or rolling during the $M_{//}$ movements when the rod aligned nearly parallel to its moving direction. This strong correlation between the rotational and translational dynamics was confirmed by results from 20 rods (Fig. 3c-d). The rods were not observed to rotate in-plane and roll simultaneously.

The $M_{//}$ movements of rods observed in our experiments agree with previous reports that tubular endosomes or mitochondria tend to align parallel to microtubules during their transport.[12, 27] This type of movement is expected, because it maximizes attachment between the rod and the microtubule tracks. The $M_{\perp}$ movements of rods are surprising, and it was unclear what could cause this unusual translational dynamics. Another question was the cause of the active rotation and rolling of the rods. To answer both questions, we simultaneously imaged rod transport and the microtubules in living cells. We first confirmed our expectation that the $M_{//}$ movements of rods correspond to their directional transport along microtubules, during which the rods are oriented parallel to the microtubule track (Fig. 4a). The $M_{//}$ movements are likely driven by dynein and kinesin, as we found that inhibition of dynein led to more immobile rods and reduced the transport speed of the mobile rods from 0.22 μm/s to 0.13 μm/s (Fig. 4d). We also observed rapid microtubule fluctuations: the filaments buckle and move laterally in a sweeping fashion, a phenomenon consistent with previous reports.[11, 28] Because of such microtubule fluctuations, rods that paused on the tracks were pushed around, appearing to move translationally in a direction perpendicular to their orientation and, simultaneously, to rotate in-plane (Fig. 4b). In such

cases, inhibition of dynein had no effect on either translational movement or in-plane rotation (Fig. 4d-e). These results indicate that the $M_{\perp}$ movements of rods and the associated in-plane rotation are both caused by forces from microtubule fluctuations. Molecular motors have negligible contributions.

In addition, we found that almost all rods (10 out of 11) that exhibited rolling motion, but little translational movement, were located in very dense network of microtubules (Fig. 4c). The inhibition of dynein again showed no effect on the rolling angle displacement (Fig. 4e), but microtubule disruption significantly reduced the rolling dynamics (Fig. S4). These results confirm that the rolling of the rods is also caused by microtubule fluctuations. Given that a rod in microtubule-dense areas is in contact with multiple microtubules, it is likely that forces exerted by fluctuating microtubules in three dimensions give rise to the rolling of the rod, but also leads to stalled translational motion. A few important conclusions can be drawn from the microtubule imaging results. First, the three types of translational behaviors of the rods have different origins. The $M_{//}$ movements are from active transport driven by molecular motors, the $M_{\perp}$ movements resulted from microtubule fluctuations, and the pauses (M_0) occur when rods are in a dense microtubule network. A rod during intracellular trafficking can exhibit all three types of movements. Second, the rotation and rolling of rods are caused by microtubule fluctuations. Rods residing on buckling microtubule filaments appear to rotate in-plane and ones in microtubule-dense areas tend to roll. This explains the correlation between the rotational and translational motion of the rods (Fig. 3).

CONCLUSION

In this study, we developed a single-rod rotational tracking method and used it to directly visualize and quantify the rotational dynamics of endosomes during intracellular transport. We fabricated Janus rods as imaging reporters that display two patches of distinct fluorescence on the opposite sides of the long axis. The shape and optical anisotropy of the Janus rods enables the simultaneous measurement of all three rotational angles (in-plane, out-of-plane, and longitudinal) and translational motion of single rods with high spatiotemporal resolutions. With the Janus rods tightly wrapped inside endosomes in cells, we uncovered a rich spectrum of in-plane rotation and rolling dynamics of endosomes that correlate with their translational transport. When the rod-containing endosomes pause on microtubules, they rotate and roll due to rapid fluctuations of the microtubule network. In contrast, endosomes undergo little rotation while being actively transported by molecular motors along microtubule tracks. The single-Janus rod tracking method allowed us to elucidate, for the first time, the rotation and rolling of rod-shaped endosomes, and more importantly the underlying driving forces. Going beyond live cell imaging of endosome dynamics, this tracking method is also expected to be a robust and useful tool for measuring rod rotation in various processes, such as during assembly at fluid interfaces and in chemically powered propulsion. Research on Janus particles has been mostly focused on their synthesis, self-assembly, design of self-propelled micromotors, and biomedical applications. In contrast, this study is one of the first few to demonstrate the potential of using Janus particles for fundamental studies in cell biology.

EXPERIMENTAL SECTION

Cells and reagents. Polyvinylpyrrolidone was purchased from TCI America (Portland, Oregon). 1-pentanol and sodium citrate dihydrate were purchased from Alfa Aesar

(Haverhill, MA).Tetraethyl orthosilicate (TEOS) was purchased from Acros (Geel, Belgium) and the ammonia was purchased from BDH (Radnor, PA). Sylgard 184 silicone elastomer kit was purchased from Dow Corning (Midland, MI). (3-Aminopropyl)triethoxysilane (APTES), biotin N-hydroxysuccinimide ester (biotin-NHS), bovine serum albumin (BSA), immunoglobulin G (IgG) from rabbit serum, colchicine, ciliobrevin A, and tannic acid were purchased from Sigma-Aldrich (St. Louis, MO). Biotinylated bovine serum albumin (BSA-biotin), Alexa Fluor 568 NHS ester, Alexa Fluor 647 NHS ester, and lipofectamine 3000 were purchased from Thermo Fisher Scientific (Waltham, MA). Branched polyethylenimine (Mw 25 kDa) was purchased from Polysciences (Warrington, PA). IgG was biotinylated with biotin-NHS and PEI was conjugated with Alexa 568 NHS ester or Alexa 647 NHS ester. DNA plasmid pCMV Fcγ RIIa IRES neo and EMTB-3×GFP were purchased from Addgene (Cambridge, MA). QIAprep Spin Miniprep Kit was purchased from Qiagen Inc (Germantown, MD). Glutaraldehyde solution (10%), osmium tetroxide solution (4%) and low viscosity embedding media Spurr's kit were purchased from Electron Microscopy Sciences (Hatfield, PA). COS-7 cells were a kind gift from Prof. Jay Groves at University of California Berkeley and originally purchased from American Type Culture Collection (Manassas, VA). COS-7 cells were cultured in DMEM complete growth media supplemented with 10% fetal bovine serum (FBS), 0.11 mg/ml (1 mM sodium pyruvate, 100 units/ml penicillin, and 100 μg/ml streptomycin). Ringer's imaging buffer (pH = 7.2, 155 mM NaCl, 5 mM KCl, 2 mM $CaCl_2$, 1 mM $MgCl_2$, 2 mM NaH_2PO_4, 10 mM HEPES, 10 mM glucose) was used for all live-cell imaging. Sodium borate buffer (pH = 8.4, 100 mM boric acid, 75 mM NaCl, 25 mM sodium tetraborate) was used for PEI incubation on

PDMS stamps during microcontact printing. LB medium (10 g/L tryptone, 5 g/L yeast extract, 10 g/L NaCl, and 100 μg/mL ampicillin) was used for E coli bacteria culture. Cytoskeleton stabilizing buffer (pH = 6.2, 500 mM NaCl, 50 mM PIPES, 15 mM MgCl2, 5 mM EGTA, 5 mM sucrose) was used for cell fixation in microtubule imaging.

Synthesis of Silica Rods. Silica rods were synthesized following a previously reported protocol.[20, 21] Briefly, 30 g polyvinylpyrrolidone (K30, Mw 40,000 g/mol) was dissolved in 300 mL 1-pentanol (98+%) in a 500 mL round bottom flask at room temperature overnight. Then 30 mL ethanol (200 proof), 8.4 mL deionized water (Millipore) and 2 mL freshly prepared sodium citrate dihydrate (99%) aqueous solution (0.18 M) were added into the polymer solution. Emulsion formed after shaking the flask by hand. To obtain uniform emulsion droplets, the emulsion solution was filtered through a polyvinylidene fluoride filter (pore size: 0.45 μm). After filtration, 6.75 mL ammonium hydroxide (28-30 wt%) and 3 mL tetraethyl orthosilicate (TEOS, 98%) were added sequentially. The solution was mixed by shaking and then left undisturbed overnight at room temperature. Silica rods grew in the emulsion droplets during this time. Silica rods were spun down at 3000 rpm for 1 hour, re-dispersed in ethanol, and then centrifuged at 2000 rpm for another 20 min. The ethanol rinsing step was repeated three times to remove most silica nanospheres. After the ethanol rinsing, silica rods were dispersed in deionized water and spun down at 1500 rpm for 15 min. The water rinsing step was repeated until the supernatant reached a neutral pH. The synthesized silica rods were 1.43 ± 0.09 μm (ave±s.d.) in length and 0.44 ± 0.06 μm (ave±s.d.) in diameter.

Fabrication of Janus rods. Silica rods were cleaned with piranha solution (H_2SO_4: 30% H_2O_2 = 3:1 v:v), rinsed with deionized water, functionalized with (3-aminopropyl)

triethoxysilane (APTES), washed with anhydrous ethanol, and then re-suspended in butanol. The rods were added to an air-water interface to self-assemble into a monolayer, which was subsequently transferred onto a silicon wafer for use.[29] To prepare the polydimethylsiloxane (PDMS) stamp for "sandwich" microcontact printing (μCP), monomer and curing agent from the Sylgard 184 silicone elastomer kit were mixed at a ratio of 10:1 (w:w) in a petri dish, degassed in a vacuum oven, and baked for 18 hours at 70 °C. PDMS stamps were cut into squares (0.7 cm×0. 7 cm×0.1 cm). To "ink" the stamps, 100 μL polyethylenimine (PEI) Alexa 568 solution (0.4 mg/mL in sodium borate buffer) was added on one side of the PDMS stamps and incubated for 20 min. After deionized water rinsing, the "inked" stamp was dried and immediately pressed against the rod monolayer. A pressure of 6×10^4 Pa was applied for 20 s before the stamp was peeled off. Rods remained partially embedded in the stamp. Subsequently, a second stamp "inked" with PEI Alexa 647 was pressed against the previous stamp with embedded rods for 20 s for printing a second patch. Janus rods were harvested by brief sonication in 2% unlabeled PEI aqueous solution. To coat the rods with immunoglobulin G (IgG), Janus rods were incubated sequentially with BSA biotin (150 μg/mL in 1×PBS buffer) for 1 hour, streptavidin (20 μg/mL in 1×PBS buffer) for 1 hour and biotinylated IgG (15 μg/mL in 1×PBS buffer) for 1.5 hours.

COS-7 cell transfection. Ampicillin-resistant E. coli (strain: DH5α) containing pCMV Fcγ RIIa IRES neo plasmid and E. coli (strain: DH5α) containing EMTB-3×GFP plasmid were purchased from Addgene in the form of agar stubs. pCMV Fcγ RIIa IRES neo plasmid was provided by Axel Nohturfft (Addgene plasmid # 14948) and EMTB-3×GFP plasmid was by William M. Bement (Addgene plasmid # 26741). [30, 31] To prepare agar plates for

bacteria growth, solution containing 10 g/L tryptone, 5 g/L yeast extract, 10 g/L NaCl, and 15 g/L agar was autoclaved and allowed to cool down to 55 ˚C. Ampicillin was subsequently added at a final concentration of 100 μg/mL. 20 mL of the mixed solution was poured into each petri dish. After solidification, the agar plates were sealed with parafilm and stored at 4 ˚C. The bacteria were streaked on agar plates with a small wooden toothpick and incubated overnight at 37 ˚C. Single colonies were isolated and inoculated in 5 mL LB medium overnight at 37 ˚C under constant shaking (150 rpm). Plasmids were extracted from the overnight culture using QIAprep Spin Miniprep Kit and stored in 10 mM Tris Buffer (pH = 8.5, Qiagen) at -4 ˚C and used within 30 days. The DNA plasmid concentration was determined by measuring the absorbance at 280 nm using a NanoDrop spectrophotometer. For long-term storage, 500 μL of the overnight culture was mixed with 500 μL of glycerol, and the mixed solution was frozen at -80 ˚C.

For cell transfection, COS-7 cells were seeded on pre-cleaned circular coverslip (diameter = 40 mm) in a plastic petri dish 24 hours before the transfection. 0.30 million COS-7 cells were seeded and on the day of transfection the confluency of the cells reached approximately 70%. Lipofectamine 3000 was used as the transfection agent. For transfection with only one type of DNA plasmid, 1.5 μg of plasmid and 5 μL of Lipofectamine 3000 were mixed in 250 μL Opti-MEM reduced serum media for 5 min. In cases of transfection with both DNA plasmids, 1 μg of Fcγ IIa receptor DNA plasmid and 1 μg of EMTB-3×GFP plasmid were mixed and used for transfection. The COS-7 cells were rinsed three times with Opti-MEM reduced serum media and kept in 2 mL Opti-MEM reduced serum media. Subsequently the 250 μL DNA-Lipofectamine mixture was added dropwise to each petri dish. The cell media and DNA plasmid solution were mixed well by

gently shaking the petri dish for 1 min. The petri dishes were centrifuged at 300 rcf for 10 min at room temperature to increase the contact between the cells and DNA plasmid before being put in incubation at 37 °C. After 3 hours of incubation, the cell medium was exchanged to serum-containing DMEM media. After overnight incubation, the cells normally reached complete confluency and were split into two petri dishes for another overnight incubation before use.

Live-cell imaging. Cells were serum starved for 4 hours and incubated with IgG-coated Janus rods for 15 min at 37 °C prior to imaging. Cells were kept in imaging buffer (pH = 7.2, 155 mM NaCl, 5 mM KCl, 2 mM $CaCl_2$, 1 mM $MgCl_2$, 2 mM NaH_2PO_4, 10 mM HEPES, 10 mM glucose) at 37 °C throughout the imaging. All live-cell imaging was finished within 45 min after addition of the Janus rods. Live-cell imaging was done using the wide-field imaging mode on a DeltaVision/OMX microscope system equipped with a 1.4NA Olympus 100× oil objective and four Photometrics Cascade II EMCCD cameras (Light Microscopy Imaging Center, Indiana University). To disrupt microtubules, cells after particle internalization were incubated with colchicine (final concentration of 200 μg/mL) for 1 hour at 37 °C before imaging.[17] To inhibit the function of molecular motor dynein, cells were incubated with ciliobrevin A (final concentration of 25 μM) at 37 °C for 30 min before live cell imaging, following a previously reported procedure.[32]

Cell fixation and immunostaining of microtubules. COS-7 cells were fixed following a cytoskeleton fixation protocol reported previously.[33, 34] To best preserve the structure of microtubules during fixation, cells were first fixed at 37 °C for 90 sec in cytoskeleton stabilizing buffer containing 0.4% (v/v) glutaraldehyde and 0.25 % (v/v) Triton-X. The cells were subsequently fixed at 37 °C for 15 min in cytoskeleton stabilizing buffer

containing 3% (v/v) glutaraldehyde. To eliminate the auto-fluorescence of glutaraldehyde, the fixed cells were incubated with freshly prepared 1×PBS buffer containing 0.5% (w/v) $NaBH_4$ for 15 min, washed three times with 1×PBS buffer, and then passivated with 1% (w/v) BSA for 45 min. Microtubules in fixed cells were labelled with DM1α antibody (500× dilution) for 30 min and then 2 μg/mL chicken-anti-mouse secondary antibody Alexa Fluor 488 for another 30 min. 1% (w/v) BSA was added during both DM1α antibody and secondary antibody functionalization steps to prevent non-specific adsorption. The immunostained cells were imaged with a Nikon A1R-A1 confocal microscope system equipped with a Nikon 100× oil-immersed objective and a Hamamatsu C11440 camera (Light Microscopy Imaging Center, Indiana University).

Transmission electron microscopy (TEM) experiments. Cell samples for TEM imaging were prepared following a previously reported protocol with slight modification.[35, 36] Cells were incubated with Janus rods at 37 °C for 45 min before trypsinization and centrifugation. The cell pellet was fixed at room temperature for 1 hour by using a mixture of 2.5% glutaraldehyde, 4% tannic acid and 2% paraformaldehyde in 1×PBS buffer. Subsequently, the pellet was rinsed three times with 1×PBS buffer and stained with 1% osmium tetroxide in 1×PBS solution for 30 min on ice. Cell pellets were dehydrated sequentially in a series of ice-cold aqueous solutions containing 30 % (v/v), 50 %, 75 %, 90 %, 95 % and 100 % ethanol for 5 minutes each. Dehydration in 100 % ethanol was repeated three times at room temperature. The dehydrated cell pellet was immersed sequentially in resin infiltration solutions that contained ethanol and Spurr's resin at various concentrations (2:1, 1:1 and 1:2, v:v) for 30 minutes each at room temperature. The cell pellet was infiltrated with 100% resin for three times, 30 min each time. Cells were

cured in 100% resin for 18 hours at 65 °C prior to microtome sectioning. Sections were stained with 2% (w/v) uranyl acetate for 10 min and 3% (w/v) lead citrate for 5 min before imaging. Samples were imaged with a JEOL JEM-1010 Transmission Electron Microscope (Electron Microscopy Center, Indiana University).

Image Analysis

(1) Image registration and noise reduction. Image registration was done to correct for optical shift between different imaging channels. 100-nm TetraSpeck fluorescent particles (ex/em: 360/430 nm, 505/515 nm, 560/580 nm, 660/680 nm) were adsorbed on polylysine-coated coverslips and the immobilized beads at a surface density of ≈ 0.05 bead/μm^2 were used as markers for image registration. After sequential imaging of the marker particles in three channels (ex: 488 nm, 561 nm, 640 nm), an affine transformation (Image J) was applied to align images from 488 nm and 561 nm channels (referred to as target images) to that from the 640 nm channel, which was used as the reference. The affine transformation uses an intensity-based subpixel registration algorithm that transforms the target images to minimize the mean-square intensity difference between the target images and reference image (Fig. S4a-b, SI). The transformations include translation, rotation, shear mapping and scaling of the target images. A global mapping matrix was obtained to record all the transformation steps and used to apply the same operations to the dual-color images of Janus rods acquired in live-cell experiments. To determine registration inaccuracy, position of individual marker beads in three channels was determined with a radial symmetry-based particle localization algorithm.[37] In theory, the identified position for each marker particle should be the same across all three channels, but in practice it shifts due to registration inaccuracy. The inter-channel shift calculated from more than 150 marker

particles from 5 images was determined to be 11± 6 nm (ave ± s.d.) for between 561 nm and 640 nm channels (Fig. S4c, SI), and 8±5 nm for between 488 nm and 640 nm channels. 11± 6 nm was used as the registration inaccuracy in our imaging experiments.

(2) Single-Janus rod tracking analysis. The xy-position and orientation of Janus rods were measured from dual-color fluorescence images using custom algorithms written in Matlab. The first step was to separate signal pixels from background in each image. All the pixels in a single fluorescence image were first estimated as either signal or background according to Otsu's method.[38] The median of all background pixels, $a(n)$, was obtained as the background level $\tilde{a}$. Standard deviation ($\hat{\sigma}$) of the background was determined using the following equation:[39]

$$\hat{\sigma} = median(|a(n) - \tilde{a}|)/0.67 \quad (1)$$

Pixels with intensity $4\hat{\sigma}$ greater than the background noise were determined as potential signals. Adjacent signal pixels were grouped together into connected components. Only connected components containing 30 or more pixels were identified as signals from a printed patch on a Janus rod and analyzed further, whereas isolated pixels were discarded. The center position of each identified patch was the intensity-weighted centroid of all signal pixels. The in-plane orientation of each identified fluorescent patch was obtained from the central image moments of its ellipse-shaped fluorescence profile using standard computer vision algorithms. Briefly, the central image moments μ_{pq} were calculated based on following equation:

$$\mu_{pq} = \sum_p \sum_q (x-\bar{x})^p (y-\bar{y})^q I(x,y) \quad (2)$$

In equation (2), p and q are integers from 0 to 2, $I(x,y)$ is the intensity of pixel (x,y), and $(\bar{x},\bar{y})$ indicates the x- and y-position of the identified centroid of a fluorescent patch. The in-plane orientation of each fluorescent patch was determined as the eigenvector associated with the larger eigenvalue for following matrix:

$$\begin{bmatrix} \mu_{20}/\mu_{00} & \mu_{11}/\mu_{00} \\ \mu_{11}/\mu_{00} & \mu_{02}/\mu_{00} \end{bmatrix}$$

Once the in-plane orientations of both fluorescent patches of a single Janus rod were identified, their average value was obtained to indicate the in-plane orientation, φ, of the entire Janus rod (Fig. 1c). This calculation results in two possible φ values that differ in π. In order to differentiate these two values, we set the imaging acquisition interval time short enough, such that the rods did not rotate more than $2/\pi$ in-plane between two consecutive frames. In image analysis, the initial orientation vector was set arbitrarily as either of the two possibilities. In all following image frames, only orientation vectors that were less than $2/\pi$ away from the previous ones were selected.

The rolling angle, θ, was calculated based the instantaneous inter-patch distance d (Fig. 1d):

$$\theta = \cos^{-1}(d/d_{max}) \quad (3)$$

In equation (3), d is the vertical distance between projection profiles of a pair of fluorescent patches on a single Janus rod, and d_{max} is the physical inter-patch distance, obtained as the maximum of d when a Janus rod samples all rolling angles during imaging. We noticed that occasionally the two fluorescent patches may not align perfectly in parallel (Fig. S1b). Therefore, d was calculated as the addition of the distance from either patch

centroid to the average in-plane orientation vector. One limitation of this method is that it cannot identify in the projected wide-field images whether the rolling angles are above or below the imaging plane.

The out-of-plane rotational angle δ can be calculated using this equation:

$$\delta = \cos^{-1}(l/l_{max}) \quad (4)$$

In equation (4), l is the length of the projected fluorescence image of a patch at any given orientation, and l_{max} is the physical length of a rod, which is obtained when a rod lie flat within the x,y plane ($\delta = 0$).

(3) Calculation of mean-square displacement (MSD) and mean-square angular displacement (MSAD). MSD was calculated as a function of lag time Δt based on the following equation:

$$\langle \Delta r^2(\tau) \rangle = \langle |r(t + \Delta t) - r(t)|^2 \rangle \quad (5)$$

In equation (5), $|r(t + \Delta t) - r(t)|$ is the end-to-end displacement of a single particle from time point t to $t + \Delta t$. Both in-plane and rolling MSAD were calculated using a similar equation, where the rotational displacement was used in place of translational displacement.

(4) Estimation of tracking uncertainty. In theory, both MSD and MSAD should be zero at Δt = 0 s for particles undergoing Brownian motion. Therefore, any non-zero y-intercepts in both plots indicate tracking uncertainty.[40] We used this principle to estimate the uncertainty of the single Janus-rod tracking analysis. To create Brownian motion of Janus rods in cells, cells were treated with a pharmacological drug colchicine that disrupts

microtubules (Fig. S2a, S2b, SI). A total of 12 particles from 6 independent samples were imaged, and their MSD and MSAD were analyzed (Fig. S2c, S2d, S2e). The first 10 points in the MSD and MSAD plots were each fitted well with a linear regression line, confirming the Brownian motion of these particles. The tracking uncertainties were determined to be 10 ± 4 nm (mean ± s.d.) for translational motion, 2 ± 1 ° (mean ± s.d.) for in-plane rotation, and 4 ± 2 ° (mean ± s.d.) for rolling.

(5) Categorization of translational and rotational motion of rods. Three different types of translational behavior were identified based on the angle α and the translational displacements. Segments of movements with end-to-end displacement > 0.5 μm within 5 sec were considered as directional motion, and ones with displacements < 0.3 μm within 5 sec considered as pauses (M_o). Among the segments of directional motion, ones with average angle α< 30° were considered as rods aligned nearly parallel to the moving direction ($M_{//}$), whereas ones with average angle α> 60° were considered as rods oriented almost perpendicularly ($M_{\perp}$). Segments of rapid unidirectional rotation (referred to as "active rotation") were distinguished from stochastic noise based on the angular displacement. The thresholds were defined as 15° within 5 s for in-plane rotation and 30° for rolling. Episodes of rotation with amplitude larger than the threshold within 5 s were considered as active rotation or rolling. The thresholds were chosen such that no active rotation or rolling of rods was detected in cells with disrupted microtubules (Fig. S5, SI).

ASSOCIATED CONTENT

Supporting Information

The Supporting Information is available free of charge on the ACS Publications website.

Details for cells and reagents, fabrication of Janus particle rods, live cell imaging, immunostaining of microtubules, TEM experiments, single-particle tracking analysis.

AUTHOR INFORMATION

Corresponding Author

*Email: yy33@indiana.edu (Y. Yu)

ACKNOWLEDGMENT

The authors gratefully acknowledge Dr. Barry Stein of the IUB Electron Microscopy Imaging Center and Dr. Jim Powers at the IUB Light Microscopy Imaging Center for assistance with instrument use. The SEM characterization of particles was done at the Nanoscale Characterization Facility at Indiana University. pCMV Fcγ RIIa IRES neo plasmid was provided by Axel Nohturfft (Addgene plasmid # 14948) and EMTB-3×GFP plasmid was by William M. Bement (Addgene plasmid # 26741). This work was supported by the National Science Foundation, Division of Chemical, Bioengineering, Environmental, and Transport Systems (Grant No. 1554078), and the Research Corporation for Science Advancement. S. M. A. acknowledges support from the Sandia National Laboratories. Sandia National Laboratories is a multimission laboratory managed and operated by National Technology and Engineering Solutions of Sandia, LLC, a wholly owned subsidiary of Honeywell International, Inc., for the U.S. Department of Energy's National Nuclear Security Administration under contract DE-NA0003525.

FIGURES AND CAPTIONS

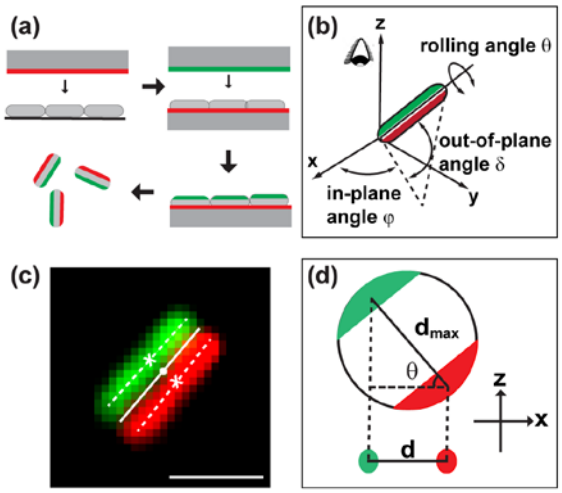

Figure 1. (a) Schematic illustration of the fabrication of Janus rods. Silica rods were first assembled into a closely packed monolayer on a silicon wafer. PEI Alexa 568 (red) and PEI Alexa 647 (green) were printed alternatively onto the opposite sides of the rods via microcontact printing. (b) A schematic showing three rotational angles of a rod to be measured in this study. The in-plane (azimuthal) angle φ is the angle between the projection of a rod on the x-y plane (imaging plane) and the x-axis. The out-of-plane (polar) angle δ is the angle between the long axis of a rod and the x-y plane. The longitudinal angle θ indicates angular change around the long axis. (c) Tracking the in-plane orientation of a single Janus rod in dual-color fluorescence images. The PEI Alexa 568 patch is in red and the PEI Alexa 647 patch is in green. The single-Janus rod tracking algorithm identifies the centroid of each fluorescent patch (indicated as the crosses) and the in-plane orientation of each patch (indicated as the dotted lines). It then determines the centroid (indicated as the solid dot) and the in-plane orientation (indicated as the solid line) of the entire Janus rod. Scale bar: 1 μm. (d) An end-view schematic showing the measurement of rolling angle θ.

The inter-patch distance of a single Janus rod in a 2D-projection in the dual-color fluorescence image is indicated as d. The maximum of d is equivalent to the physical inter-patch distance d_{max}.

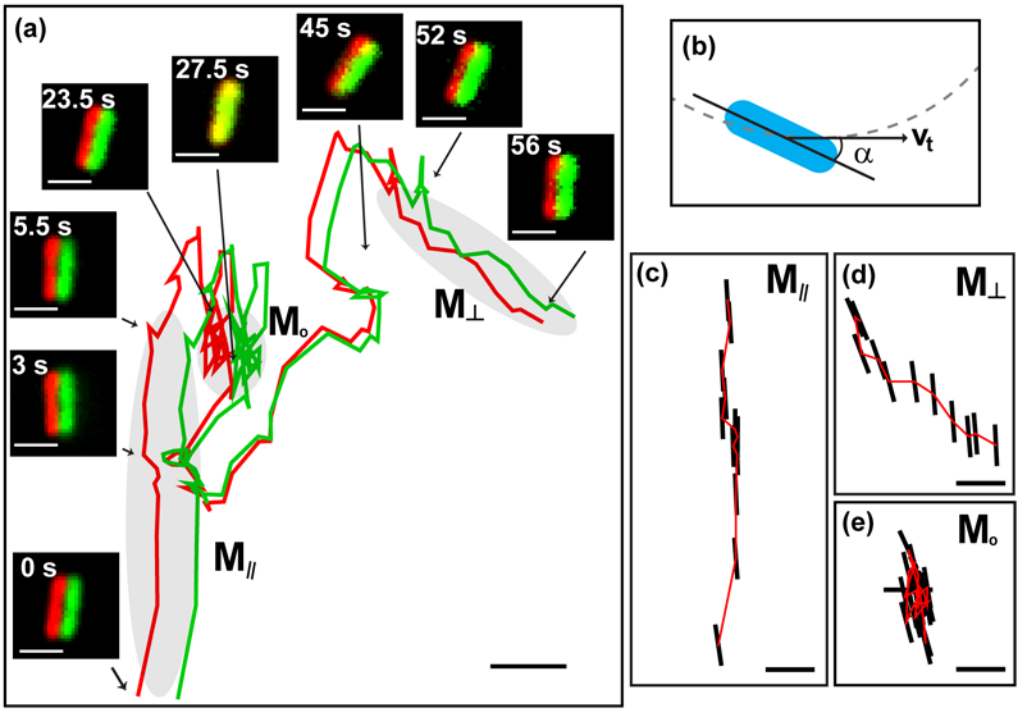

Figure 2. (a) The trajectories of the two fluorescent patches of a representative Janus rod in a cell. Insets are dual-color fluorescence images of the Janus rod at different elapsed times as indicated. Two patches are shown in red and green, and their overlapping area is shown in yellow. Gray shades highlight representative segments of three types of translational behaviors: movements during which rods are oriented nearly parallel ($M_{//}$) or perpendicular ($M_{\perp}$) to the moving direction, and pauses of rods (M_{o}). For clarity, the inter-patch distance of the trajectories is scaled down to 25% of the original distance. Scale bar: 100 nm. Scale bar of the insets: 1 μm. The trajectory is representative of >50 rods analyzed. b) Schematic illustration of the definition of angle α, the angle between the long axis of

the rod and the instantaneous moving velocity v_t. (c-e) Rod orientation (shown as short black lines) overlaid with trajectories (shown as red lines) of the $M_{//}$ movements (0 s to 5.5 s), $M_{\perp}$ movements (52 s to 57 s), and the M_o pause (16 s to 27 s) as highlighted by the gray shades in panel 2a. Scale bars: 100 nm.

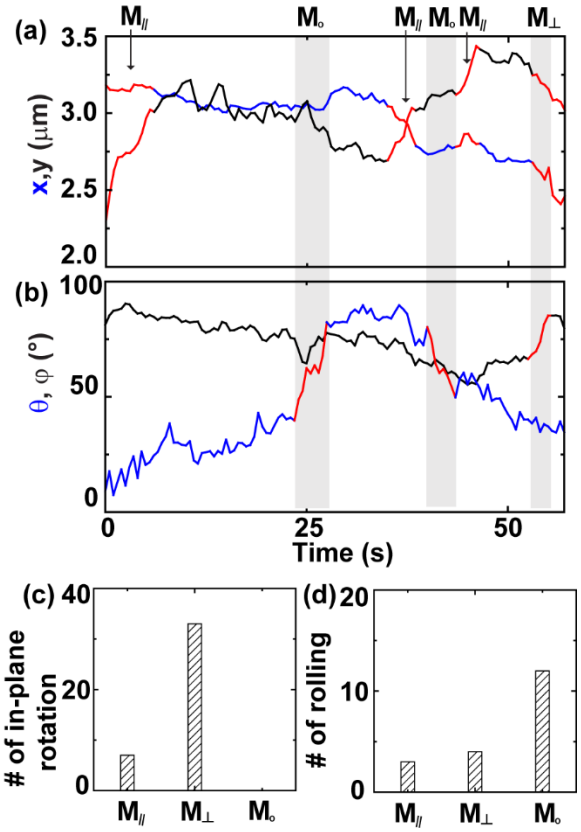

Figure 3. (a) X-displacement (blue) and y-displacement (black) of the rod shown in Fig. 2a are plotted against time. Segments of the $M_{//}$ and $M_{\perp}$ movements are labelled in red. Gray shades indicate pauses (M_o). (b) The rolling angle θ (blue) and the in-plane angle φ (black) of the rod shown in Fig. 2a are plotted against time. The active rolling and in-plane rotation are labelled in red in the shaded area. (c-d) Histograms showing the occurrence of the in-plane rotation (c) and rolling (d) during the three types of translatioinal behaviors as

indicated. Data include a total of 40 active in-plane rotational events and 19 active rolling events from 20 Janus rods.

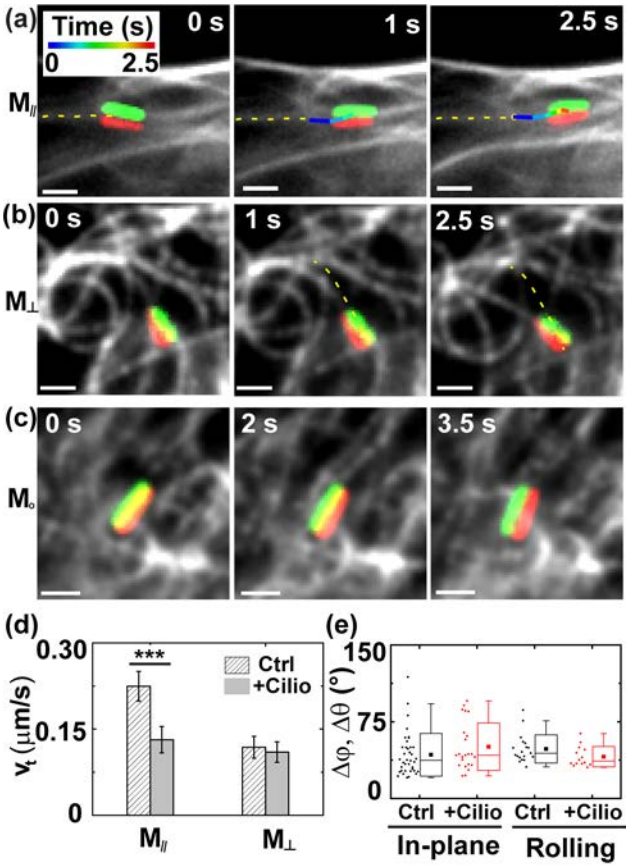

Figure 4. (a-c) Overlaid fluorescence images showing Janus rods and underlying microtubules during the $M_{//}$ movements (a), $M_{\perp}$ movements (b), and M_o pauses (c). In all images, the two fluorescent patches on Janus rods are shown in red and green, and their overlapping areas are shown in yellow. Microtubules in cells are shown in gray. Trajectories of the rods are color-coded with time according to the color bar. Each set of images are representative of > 10 rods in cells. The yellow dash lines in (a) highlight the microtubule track that the rod moves on and those in (b) highlight the morphology of the

microtubule track at 0 s. Scale bars: 1 μm. (d) Bar graphs showing the translational speeds of Janus rods during $M_{//}$ and $M_{\perp}$ movements in cells with dynein inhibition (+Cilio) or without (Ctrl). The error bars represent standard error. Statistical significance is highlighted by the p-value (student's t test) as follows: ***$p < 0.001$. Data include 70 $M_{//}$ segments and 65 $M_{\perp}$ segments from 20 rods in control cells, and 55 $M_{//}$ segments and 40 $M_{\perp}$ segments from 20 rods in ciliobrevin-treated cells. (e) Box and scatter plots showing the angular displacements of the in-plane rotation and rolling of rods in control cells (Ctrl, shown in black) or in cells with dynein inhibition (+Cilio, shown in red). Data within each group are not significantly different, as shown by student's t-test. Data include 40 active in-plane rotational events and 19 active rolling events from 20 rods for the control group, and 23 active in-plane rotational events and 14 active rolling events from 20 rods for the ciliobrevin-treated group.

REFERENCES:

1. Gross, S. P. Hither and yon: a review of bi-directional microtubule-based transport. *Phys. Biol.* **2004,** *1* (2), R1-R11.
2. Hancock, W. O. Bidirectional cargo transport: moving beyond tug of war. *Nat. Rev. Mol. Cell Biol.* **2014,** *15* (9), 615-628.
3. Ross, J. L.; Ali, M. Y.; Warshaw, D. M. Cargo transport: molecular motors navigate a complex cytoskeleton. *Curr. Opin. Cell Biol.* **2008,** *20* (1), 41-47.
4. Welte, M. A. Bidirectional transport: matchmaking for motors. *Curr. Biol.* **2010,** *20* (9), R410-R413.
5. Chevalier-Larsen, E.; Holzbaur, E. L. Axonal transport and neurodegenerative disease. *Biochim. Biophys. Acta* **2006,** *1762* (11), 1094-1108.
6. De Vos, K. J.; Grierson, A. J.; Ackerley, S.; Miller, C. C. Role of axonal transport in neurodegenerative diseases. *Annu. Rev. Neurosci.* **2008,** *31*, 151-173.
7. Kusumi, A.; Tsunoyama, T. A.; Hirosawa, K. M.; Kasai, R. S.; Fujiwara, T. K. Tracking single molecules at work in living cells. *Nat. Chem. Biol.* **2014,** *10* (7), 524-532.
8. Ruthardt, N.; Lamb, D. C.; Bräuchle, C. Single-particle tracking as a quantitative microscopy-based approach to unravel cell entry mechanisms of viruses and pharmaceutical nanoparticles. *Mol. Ther.* **2011,** *19* (7), 1199-1211.
9. Saxton, M. J.; Jacobson, K. Single-particle tracking: applications to membrane dynamics. *Annu. Rev. Biophys. Biomol. Struct.* **1997,** *26* (1), 373-399.
10. Kural, C.; Kim, H.; Syed, S.; Goshima, G.; Gelfand, V. I.; Selvin, P. R. Kinesin and dynein move a peroxisome in vivo: a tug-of-war or coordinated movement? *Science* **2005,** *308* (5727), 1469-1472.
11. Kulić, I. M.; Brown, A. E.; Kim, H.; Kural, C.; Blehm, B.; Selvin, P. R.; Nelson, P. C.; Gelfand, V. I. The role of microtubule movement in bidirectional organelle transport. *Proc. Natl. Acad. Sci. U.S.A.* **2008,** *105* (29), 10011-10016.
12. Zajac, A. L.; Goldman, Y. E.; Holzbaur, E. L.; Ostap, E. M. Local cytoskeletal and organelle interactions impact molecular-motor-driven early endosomal trafficking. *Curr. Biol.* **2013,** *23* (13), 1173-1180.
13. Kulkarni, R. P.; Castelino, K.; Majumdar, A.; Fraser, S. E. Intracellular transport dynamics of endosomes containing DNA polyplexes along the microtubule network. *Biophys. J.* **2006,** *90* (5), L42-L44.
14. Soppina, V.; Rai, A. K.; Ramaiya, A. J.; Barak, P.; Mallik, R. Tug-of-war between dissimilar teams of microtubule motors regulates transport and fission of endosomes. *Proc. Natl. Acad. Sci. U.S.A.* **2009,** *106* (46), 19381-19386.
15. Xiao, L.; Qiao, Y.; He, Y.; Yeung, E. S. Imaging translational and rotational diffusion of single anisotropic nanoparticles with planar illumination microscopy. *J. Am. Chem. Soc.* **2011,** *133* (27), 10638-10645.
16. Chaudhari, K.; Pradeep, T. Spatiotemporal mapping of three dimensional rotational dynamics of single ultrasmall gold nanorods. *Sci. Rep.* **2014,** *4*.
17. Gu, Y.; Sun, W.; Wang, G.; Jeftinija, K.; Jeftinija, S.; Fang, N. Rotational dynamics of cargos at pauses during axonal transport. *Nat. Commun.* **2012,** *3*, 1030.
18. Polishchuk, R. S.; Capestrano, M.; Polishchuk, E. V. Shaping tubular carriers for intracellular membrane transport. *FEBS Lett.* **2009,** *583* (23), 3847-3856.
19. Saxton, W. M.; Hollenbeck, P. J. The axonal transport of mitochondria. *J. Cell Sci.* **2012,** *125* (9), 2095.
20. Kuijk, A.; van Blaaderen, A.; Imhof, A. Synthesis of Monodisperse, Rodlike Silica Colloids with Tunable Aspect Ratio. *J. Am. Chem. Soc.* **2011,** *133* (8), 2346-2349.

21. Kuijk, A.; Imhof, A.; Verkuijlen, M. H.; Besseling, T. H.; van Eck, E. R.; van Blaaderen, A. Colloidal silica rods: Material properties and fluorescent labeling. *Part. Part. Syst. Char*. **2014,** *31* (6), 706-713.
22. Jiang, S.; Granick, S. A Simple Method to Produce Trivalent Colloidal Particles. *Langmuir* **2009,** *25* (16), 8915-8918.
23. Sanchez, L.; Patton, P.; Anthony, S. M.; Yi, Y.; Yu, Y. Tracking single-particle rotation during macrophage uptake. *Soft Matter* **2015,** *11* (26), 5346-5352.
24. Aderem, A.; Underhill, D. M. Mechanisms of phagocytosis in macrophages. *Annu. Rev. Immunol.* **1999,** *17*, 593-623.
25. Swanson, J. A.; Hoppe, A. D. The coordination of signaling during Fc receptor-mediated phagocytosis. *J. Leukoc. Biol.* **2004,** *76* (6), 1093-1103.
26. Hendricks, A. G.; Perlson, E.; Ross, J. L.; Schroeder, H. W.; Tokito, M.; Holzbaur, E. L. Motor coordination via a tug-of-war mechanism drives bidirectional vesicle transport. *Curr. Biol.* **2010,** *20* (8), 697-702.
27. Misgeld, T.; Kerschensteiner, M.; Bareyre, F. M.; Burgess, R. W.; Lichtman, J. W. Imaging axonal transport of mitochondria in vivo. *Nat. Methods* **2007,** *4* (7), 559-561.
28. Brangwynne, C. P.; MacKintosh, F.; Weitz, D. A. Force fluctuations and polymerization dynamics of intracellular microtubules. *Proc. Natl. Acad. Sci. U.S.A.* **2007,** *104* (41), 16128-16133.
29. Chen, Q.; Diesel, E.; Whitmer, J. K.; Bae, S. C.; Luijten, E.; Granick, S. Triblock Colloids for Directed Self-Assembly. *J. Am. Chem. Soc.* **2011,** *133* (20), 7725-7727.
30. Trivedi, V.; Zhang, S. C.; Castoreno, A. B.; Stockinger, W.; Shieh, E. C.; Vyas, J. M.; Frickel, E.-M.; Nohturfft, A. Immunoglobulin G signaling activates lysosome/phagosome docking. *Proc. Natl. Acad. Sci. U.S.A.* **2006,** *103* (48), 18226-18231.
31. Miller, A. L.; Bement, W. M. Regulation of cytokinesis by Rho GTPase flux. *Nat. Cell Biol.* **2009,** *11* (1), 71-77.
32. Firestone, A. J.; Weinger, J. S.; Maldonado, M.; Barlan, K.; Langston, L. D.; O'Donnell, M.; Gelfand, V. I.; Kapoor, T. M.; Chen, J. K. Small-molecule inhibitors of the AAA+ ATPase motor cytoplasmic dynein. *Nature* **2012,** *484* (7392), 125-129.
33. Whelan, D. R.; Bell, T. D. Image artifacts in Single Molecule Localization Microscopy: why optimization of sample preparation protocols matters. *Sci. Rep.* **2015,** *5*, 7924.
34. Xu, K.; Zhong, G.; Zhuang, X. Actin, spectrin, and associated proteins form a periodic cytoskeletal structure in axons. *Science* **2013,** *339* (6118), 452-456.
35. Van Deurs, B. The use of a tannic acid—glutaraldehyde fixative to visualize gap and tight junctions. *J. Ultrastruct. Res.* **1975,** *50* (2), 185-192.
36. Schrand, A. M.; Schlager, J. J.; Dai, L.; Hussain, S. M. Preparation of cells for assessing ultrastructural localization of nanoparticles with transmission electron microscopy. *Nat. Protoc.* **2010,** *5* (4), 744-757.
37. Parthasarathy, R. Rapid, accurate particle tracking by calculation of radial symmetry centers. *Nat. Methods* **2012,** *9* (7), 724-726.
38. Otsu, N. A threshold selection method from gray-level histograms. *Automatica* **1975,** *11* (285-296), 23-27.
39. Sadler, B. M.; Swami, A. Analysis of multiscale products for step detection and estimation. *IEEE Trans. Inf. Theory* **1999,** *45* (3), 1043-1051.
40. Anthony, S. M.; Hong, L.; Kim, M.; Granick, S. Single-particle colloid tracking in four dimensions. *Langmuir* **2006,** *22* (24), 9812-9815.

Table of Content (TOC)